

# Chapter 8

## Data

### 8.1 Overview

The experiment's commissioning run was in 2001. The first sets for muon decay parameter extraction were acquired in 2002, and results for  $\rho$  and  $\delta$  were published in 2005[39, 41]. An engineering run took place in 2003, followed by the second set of physics data in 2004. The 2004 data has been analysed twice: the first publication in 2006 was for  $P_\mu^\pi \xi$ [36], and the second publication in 2008 was for  $\rho$  and  $\delta$ [38].

The author commenced studies in September 2005, and the experiment soon undertook an engineering run from October 2005 to December 2005. Data was accumulated that had the potential for physics results, but was not analysed for this purpose<sup>40</sup>.

The data analysed for this thesis was acquired in two periods: muons were stopped in a silver target from October 2006 to December 2006, and in an aluminium target from May 2007 to August 2007. From June 2006 to September 2006 data was accumulated on the same aluminium target, but this was not analysed<sup>41</sup>.

### 8.2 Muon beam from chamber measurements

The muon beam spots at each pair of DCs and PCs were used to tune the beam line and later reject runs due to instabilities. The characterisation of this internal muon beam will now be described.

The trajectories of two muons are shown in Fig. 8.1, where a muon with small and large momentum components transverse to the  $z$  direction are considered. Figure 8.1(c) shows the magnitude of the magnetic field along  $x = y = 0$ , with the drift chamber tracking region marked. Individual muon trajectories could not be reconstructed using the drift chambers due

---

<sup>40</sup>Instead the aim was to study effects such as exaggerated stops in the chamber gas, practice steering the muon beam to maximise transverse momentum and fringe field depolarisation, and obtain new data for muons stopping immediately at the entrance of the detector.

<sup>41</sup>Unfortunately two metal spanners were accidentally left inside the detector over this period, affecting the tracking field in a way that could not be easily corrected. In other words, it was less effort to re-take the data in 2007.

to the muons having low transverse momentum, significant energy loss and more crosstalk.

The average position of the muon beam is better behaved, and is shown for  $10^4$  muons in Figs. 8.2(a) and 8.2(c). Inside the tracking region the beam appears to be well described by a helix with decaying amplitude and wavelength.

At each pair of orthogonal planes a muon beam spot is made, and if the mean positions of each beam spot are plotted against  $z$ , the result is Figs. 8.2(b) and 8.2(d). Note in this figure the  $z$  coordinate is redefined as  $z' = z + 59.59$ , so that  $z' = 0$  corresponds to the first pair of planes encountered (PC1 and PC2). A best fit is included according to

$$\begin{pmatrix} \langle x \rangle \\ \langle y \rangle \end{pmatrix} = (A - A_d \cdot z') \begin{pmatrix} \cos(f(z')) \\ \sin(f(z')) \end{pmatrix} + \begin{pmatrix} \Delta_x \\ \Delta_y \end{pmatrix}, \quad (8.1)$$

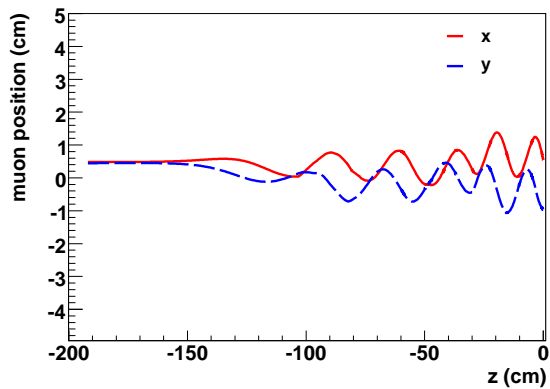
$$(8.2)$$

where  $\langle x \rangle$  and  $\langle y \rangle$  are the mean muon positions,  $\Delta_x$  and  $\Delta_y$  are the positions of the helix centre,  $A$  is the amplitude of the helix at  $z' = 0$ ,  $A_d$  is a linear decay parameter, and

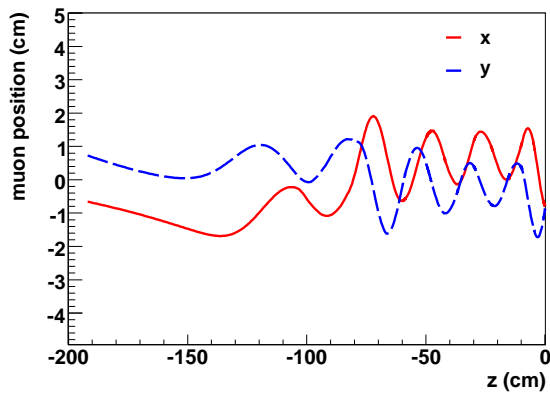
$$f(z') = 2\pi \frac{z'}{\lambda - \lambda_d z'} + \phi, \quad (8.3)$$

where  $\lambda$  is the helix wavelength at  $z' = 0$ ,  $\phi$  is the phase at  $z' = 0$  and  $\lambda_d$  is a linear decay parameter. The parameters  $A$  and  $\lambda$  approximately correspond to average transverse and longitudinal momentum.

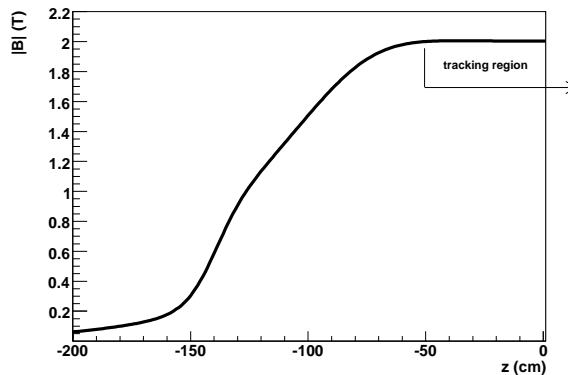
Equation 8.2 is fit to the mean position at all chambers except the final proportional chambers and the last two pairs of drift chambers. This gives a total of 11 points, from which 7 fit parameters are determined. In a typical fit the correlation coefficients are below 0.8 except for the correlation between  $\lambda$  and  $\lambda_d$ , which is generally greater than 0.95. Trials were carried out where Eq. 8.2 allowed for an angular rotation in the  $x$  and  $y$  planes. However the angles determined from this approach were uncompetitive with alternative alignment methods.



(a) Trajectory for a muon with small transverse momentum.

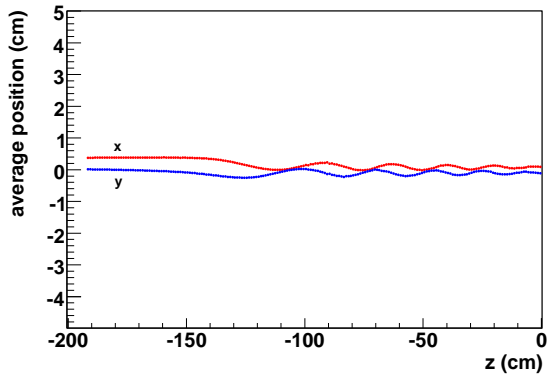


(b) Trajectory for a muon with large transverse momentum.

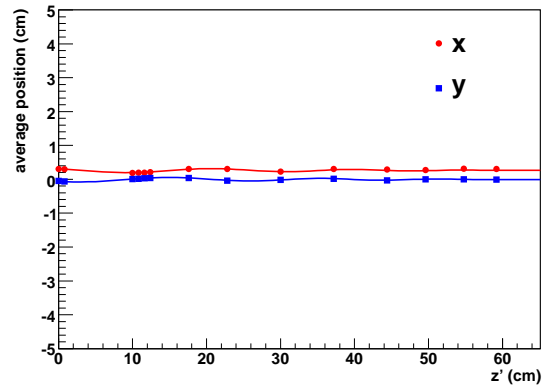


(c) Magnitude of the magnetic field at  $x = y = 0$ .

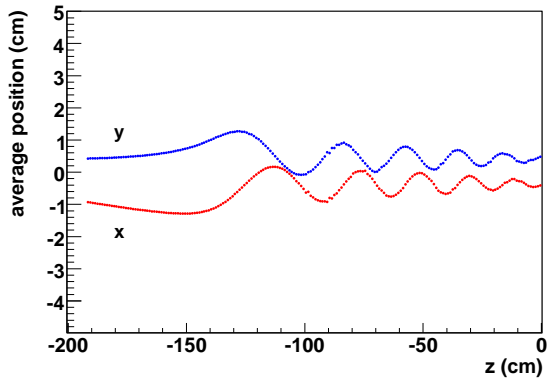
Figure 8.1: Individual muon trajectories for a low and high transverse momentum scenario. The magnitude of the magnetic field is included for convenience.



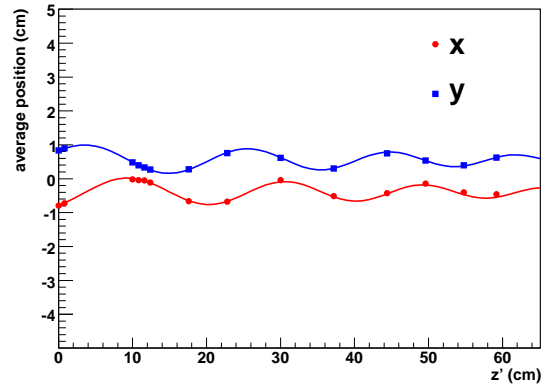
(a) Average position for a beam with small transverse momentum.



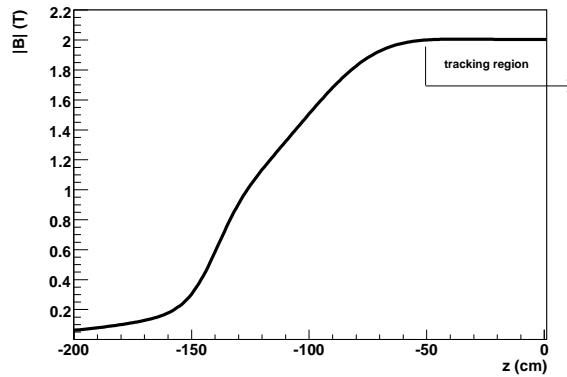
(b) Average position, tracking region only.



(c) Average position for a beam with large transverse momentum.



(d) Average position, tracking region only.



(e) Magnitude of the magnetic field at  $x = y = 0$ .

Figure 8.2: The position of  $10^4$  muons at 1 cm intervals is plotted for a low and high average transverse momentum beam. The magnitude of the magnetic field is included for convenience.

### 8.3 Muon beam tuning

The muon beam was tuned using the TECs, which measured individual muon trajectories before the solenoidal field, and the internal beam that was described in the previous section.

A muon beam directed along the magnetic field axis with minimised transverse momentum will have the highest polarisation. This beam is claimed to have the smallest polarisation uncertainty since it experiences minimal transverse magnetic field components, and is more robust to angle and position misalignments of the original beam. Originally the aim was to tune the beam line for a total depolarisation of  $\lesssim 1 \times 10^{-4}$ . However, this could not be achieved with a sensible rate, and instead a depolarisation  $\approx 30 \times 10^{-4}$  was achieved.

At the time of beam tuning, the TECs were not calibrated or aligned, allowing only an approximate measure of the beam's position and angle. The muon beam was steered to be roughly on axis, with small average angle, using the quadrupole steering that was described in Section 3.4. The beam inside the detector was then tuned to have minimal transverse momentum. Even though the chambers were not aligned at this stage, their relative placement was known with higher precision than the removeable TECs. An example of the beam spots inside the detector after tuning, including their RMS size, is shown in Fig. 8.3.

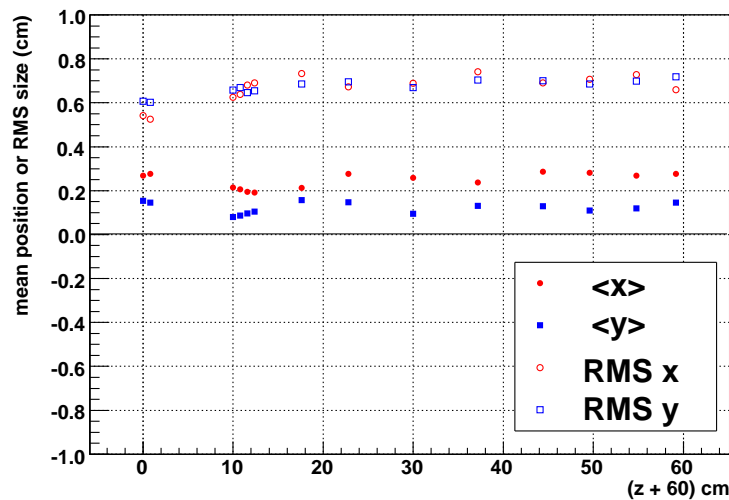


Figure 8.3: Muon beam inside the detector, after tuning.

## 8.4 Data sets

Data was accumulated in “sets” of  $\approx 0.9 \times 10^9$  events, which appear in chronological order in Table 8.1. The individual sets were three times larger than the previous  $P_\mu^\pi \xi$  measurement, each requiring about six days of continuous acquisition. The increased statistics,  $\approx 8 \times 10^9$  events before cuts compared to  $1.5 \times 10^9$  previously, are necessary for  $\rho$  and  $\delta$ ;  $P_\mu^\pi \xi$  is instead dominated by systematic uncertainties.

Table 8.1 shows there were two nominal sets accumulated on each target, where the initial muon momentum was 29.6 MeV/c, the stopping distribution was peaked at the centre of the target, the uniform magnetic field was at 2.0 T, and the downstream beam package was *not* in place (see Section 3.10).

There were sets taken as consistency checks: the different stopping distribution checks the momentum calibration, the B= 1.96 T and B=2.04 T sets were tests of the magnetic field’s effect on reconstruction, and the downstream beam package was used to check that backscatters were properly simulated. Special sets were taken to evaluate  $P_\mu^\pi \xi$  systematic uncertainties; two sets had the beam steered to lower polarisation, as shown in Figs. 8.2(c) and 8.2(d), and two sets had the TECs in place during data acquisition. A set was taken at lower momentum, which corresponds to selecting muons from deeper within the production target. This exaggerates the production target multiple scattering that is not included in the simulation.

There were also sets where the muons were stopped immediately after the muon counter, and the decay positron was reconstructed independently in each half of the detector. This data was taken on the standard silver and aluminium targets, and a special large radius aluminium target that allowed the relaxation of certain analysis cuts. These sets were used as precise checks of the positron interactions in the target, which are important for improving the systematic uncertainties that dominate the  $\rho$  and  $\delta$  measurements.

There was other data accumulated to align the chambers in position and angle, calibrate the timing offsets, determine the STRs for the time expansion chambers, tune the muon beam and calibrate the channel momentum. The time expansion chambers were inserted to measure the muon beam at the start and end of each set.

Table 8.1: Data sets accumulated in 2006/2007, in chronological order. The number of fiducial events is shown for the sets used to extract  $\Delta P_{\mu}^{\pi} \xi$ .

Target	Description	Number of events ( $\times 10^6$ )		
		Before quality checks	Before cuts/ selections	In fiducial
Ag	Stopping distrib. peaked $\frac{1}{3}$ into target	741	587	?
Ag	B = 1.96 T	952	790	-
Ag	B = 2.04 T	879	765	-
Ag	TECs-in, nominal beam	926	842	-
Ag	Muons stopped far upstream	1113	1036	-
Ag	Nominal A	580	506	43
Ag	Nominal B	834	787	66
Ag	Low polarisation	685	635	-
Al	Muons stopped far upstream	363	274	-
Al	TECs-in, spread beam	861	612	-
Al	Downstream beam package in place	943	850	62
Al	Nominal C	1029	746	33
Al	Low polarisation	1099	1036	-
Al	Nominal D	854	798	55
Al	Lower momentum	1129	952	?
Large Al	Muons stopped far upstream	708	495	-

## 8.5 Data quality checks

The previous  $P_{\mu}^{\pi} \xi$  measurement could not rule out muon beam instabilities as the cause of the dominant systematic uncertainty. The abundant statistics for the current round of measurements allowed extremely conservative rejection of suspicious data, which will now be described. For the following sections, note that a data set was accumulated in approximately 900 “runs” of nominal size 2 GB.

### 8.5.1 Data acquisition system

The DAQ (data acquisition system) included the TDCs described in Section 3.12, and the computer to which they were interfaced. This computer used the software MIDAS. Runs were excluded due to the following DAQ problems:

- TDCs sometimes received too much information due to an electronics problem, and become out-of-synchronisation with the others. This was more common while the TECs were in place.
- A TDC would sometimes stop responding.
- A TDC channel could temporarily become corrupt.
- The computer’s event accumulating software would sometimes crash.
- The computer could fail to make a database entry for a run, or write a run with zero events.
- While data was accumulating, a periodic pulser signal was added that could be subsequently analysed to make sure all the TDCs were operating correctly. If a run contained more than three pulser problems it was eliminated.

Any run that completed with too few events was conservatively eliminated. Additionally the number of events in a run was used identify and reject periods where the DAQ was unstable.

### 8.5.2 Chamber signals

During maintenance periods when the proton beam was off, the detector was “opened up” to carry out maintenance such as broken wire repairs, or changing the target foil. This took place in a special clean room, but some contamination due to dust was inevitable. In the days following such a maintenance period the current or voltage in a chamber occasionally

exceeded a threshold and the run was stopped; the cause was believed to be residual dust, and these runs were eliminated. More seriously, after maintenance the pre-amplifiers sometimes suffered “electrical oscillations”, and produced signals that overloaded the DAQ. This could make the detector unusable for hours while post amplifier thresholds were adjusted. The periods of time where this occurred were eliminated.

### 8.5.3 Rates

The DAQ computer recorded several accumulated counts:

- A halo counter surrounding the production target, which was proportional to the protons delivered, and was used to normalise the other counts.
- The number of upstream triggers from the muon-counter.
- The number of upstream triggers in the annular counter that surrounded the muon-counter (see Section 3.10).
- The number of downstream triggers from the new downstream scintillator, which included muons, beam positrons and decay positrons.

The counts were converted into normalised rates using the halo counter, and used to eliminate periods of instability. An example is shown in Fig. 8.4.

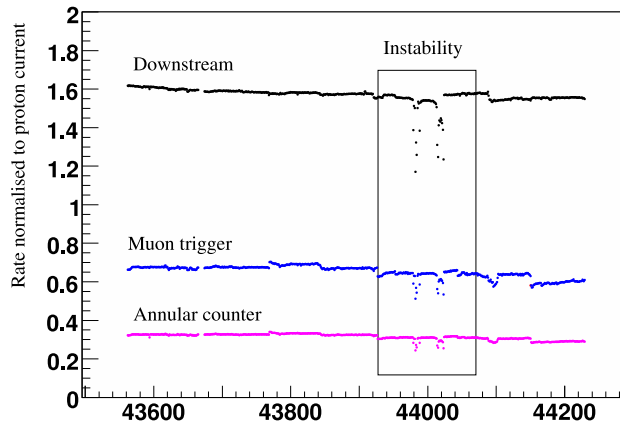


Figure 8.4: Example of a period when the rates were unstable.

### 8.5.4 Beam line stability

Section 3.2.3 described the M13 beam line in detail. The DAQ recorded the currents and voltages across the M13 elements (dipoles, quadrupoles), and the positions of the slits and jaws.

NMRs on the dipoles allowed the field to be automatically regulated to  $< 0.01$  mT. Occasionally a regulator was not set properly by the operator, or the beam line settings were accidentally changed during a set, or the NMR signal became weak. Such occurrences were easily detected, and the runs eliminated.

There were periods where the operator observed instabilities in several of the beamline quadrupoles (Q4, Q6, Q7). Some of these instabilities were readback errors, and therefore had no effect on the muon beam. The known genuine instabilities were eliminated, but the questionable runs were kept at this stage, and investigated more carefully using the muon beam itself (see Section 9.8).

### 8.5.5 Chamber foil bulging

Recall from Section 3.8 that the chamber gases were vented to the atmosphere. A difference between the temperature in the experimental hall, and the slowly changing internal temperature, led to a change in STR relationship due to the chamber foils bulging. For an acceptable systematic uncertainty the bulge had to be  $< 50$   $\mu\text{m}$ . A temperature difference of  $3^\circ\text{C}$  was tolerated, which corresponded to a bulge of  $35$   $\mu\text{m}$ . The operators maintained this difference by adjusting the air flow to the experimental hall, and were successful since only 10% of one set had to be excluded. The systematic uncertainty due to the small bulging is described in Section 9.2.2.

### 8.5.6 Muon stopping distribution

Section 3.10 described a chamber in which the  $\text{CO}_2$  and He concentration could be adjusted to control the muon range. This adjustment was automated by analysing a sample of the muons while accumulating data, and maintaining the average last position at which the muon was seen. Runs were rejected if this average was outside of statistical fluctuations.

### 8.5.7 Problems observed by operator

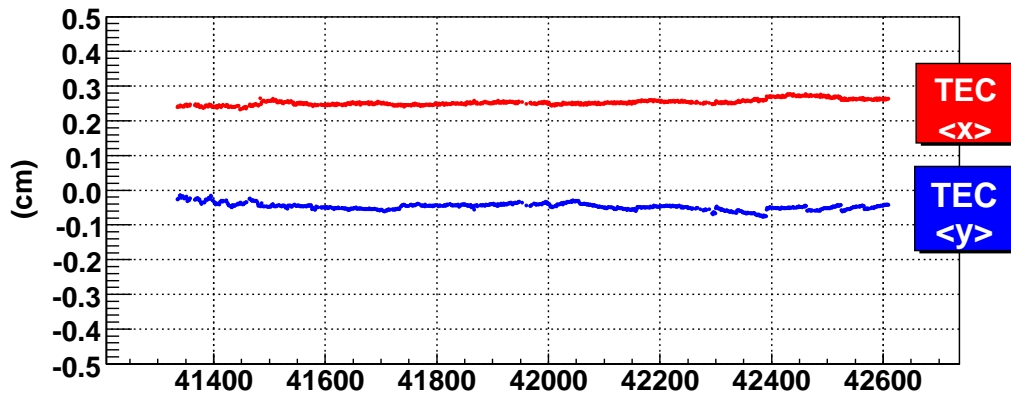
Runs were excluded based on operator concerns and observations.

### 8.5.8 Muon beam stability

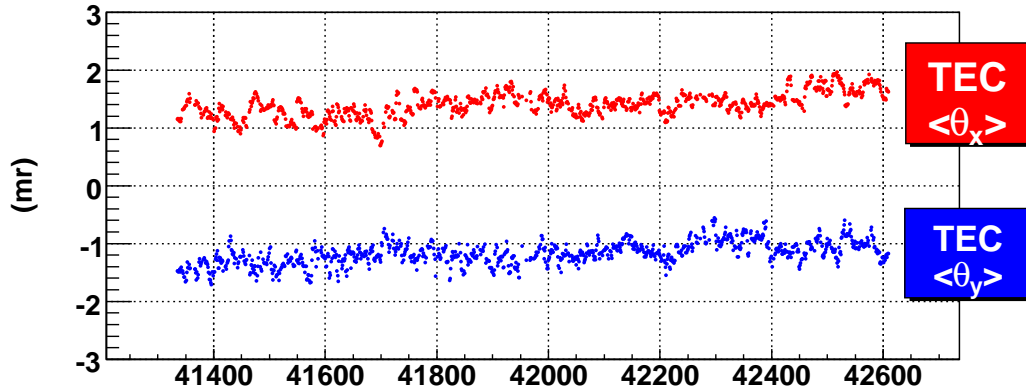
The set with the nominal beam tune and TECs in place allowed a high precision measurement of the muon beam stability. The average positions and angles from the TECs and the internal beam ( $\Delta_x, \Delta_y$ ) are shown in Fig. 8.5. The beam position was stable to  $< 0.1$  cm, and the angles to  $< 1$  mr, which are negligible variations. Unsurprisingly the internal beam parameters had no sensitivity to these small changes in TEC parameters. Unfortunately for this set the transverse momentum was too small to reliably reconstruct the other internal beam parameters ( $A$ ,  $\lambda$  and  $\phi$ ).

The internal beam was carefully examined for every data set. For five sets the beam had very low transverse momentum, and only the position of the internal beam was meaningful. Figure 8.6 is an example where all the internal beam parameters are available, and it demonstrates the stability of the internal muon beam; the position is notably stable to  $< 0.02$  cm, but subject to small systematic steps. The TEC characterisations from the start and end of each set allow an upper limit on the change in polarisation due to these steps ( $0.8 \times 10^{-4}$  in this case). The systematic uncertainty is considered more carefully in Section 9.8.

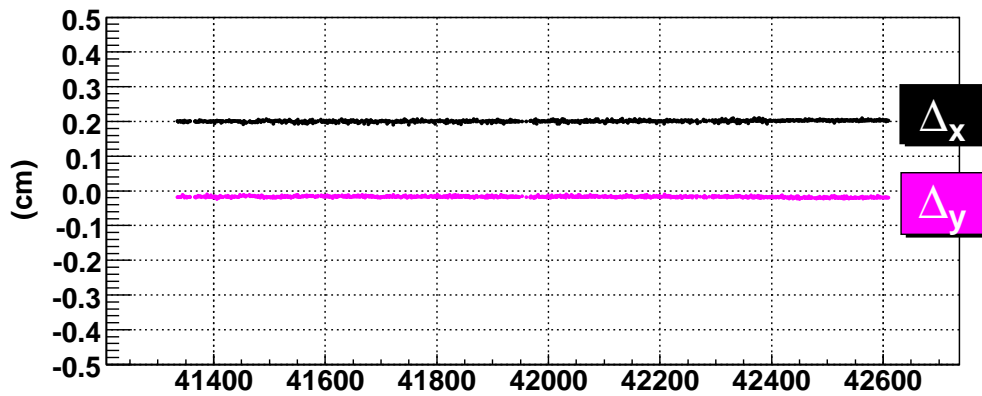
The examination of the internal beam led to several important conclusions. Firstly the set with the most stable internal beam had the largest change in start/end-of-set TEC characterisations. This strongly suggests that TEC non-reproducibility dominates any systematic uncertainty from muon beam instability. Secondly the low polarisation sets were found to be stable, which will be important when the fringe field systematic uncertainty is determined in Chapter 9. Lastly a handful of runs were excluded due to clear changes in the internal beam.



(a) TEC average position.

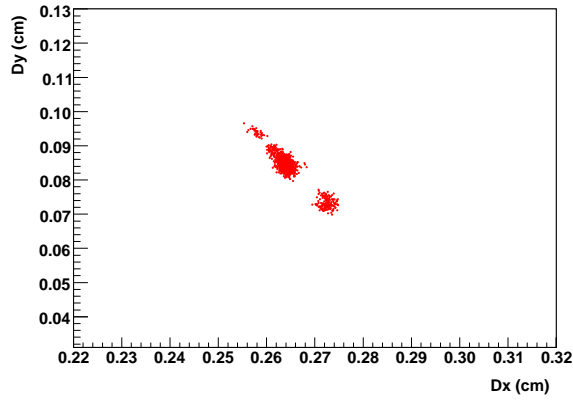


(b) TEC average angle.

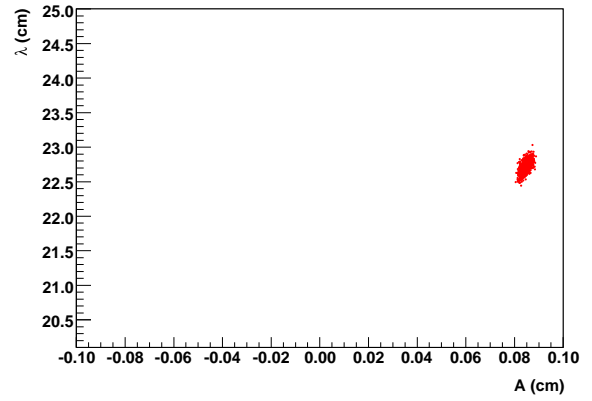


(c) Internal beam position.

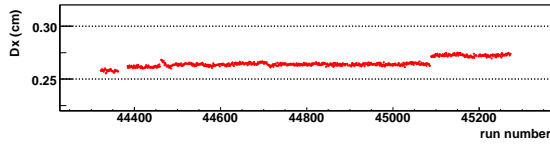
Figure 8.5: Beam parameter averages for the set with TECs in place.



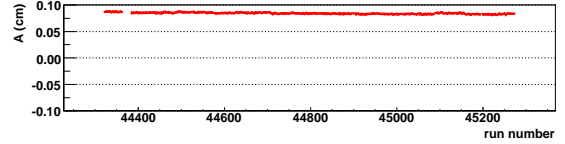
(a)  $(\Delta_x, \Delta_y)$ .



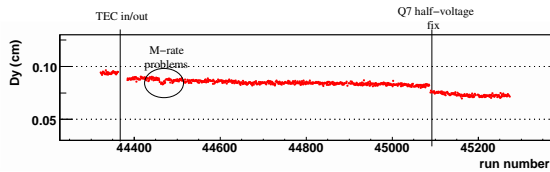
(b) Amplitude,  $A$  and wavelength  $\lambda$ .



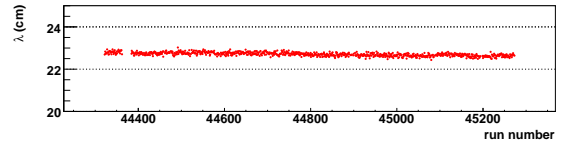
(c) Stability of  $\Delta_x$ .



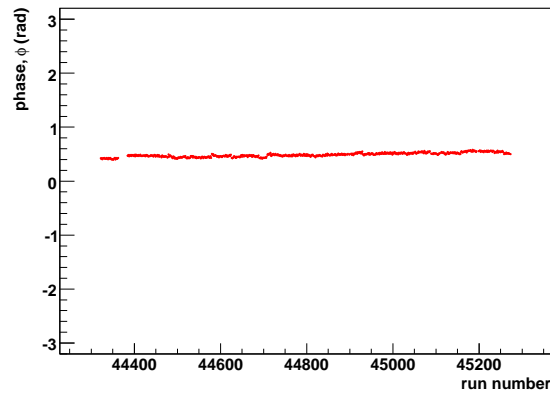
(d) Stability of  $A$ .



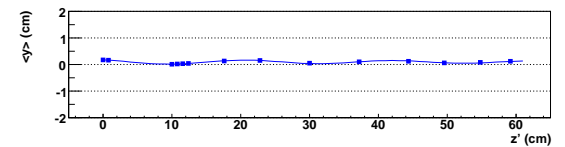
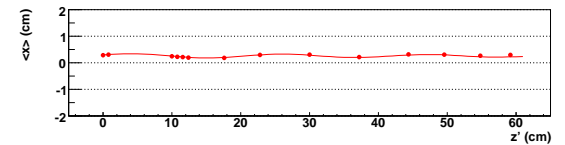
(e) Stability of  $\Delta_y$ .



(f) Stability of  $\lambda$ .



(g) Stability of  $\phi$ .



(h) Example decaying helix fit.

Figure 8.6: Internal beam stability for nominal B.